View Article Online
View Journal

PCCP

Physical Chemistry Chemical Physics

Accepted Manuscript

This article can be cited before page numbers have been issued, to do this please use: M. Jabbarzadeh Sani, *Phys. Chem. Chem. Phys.*, 2025, DOI: 10.1039/D5CP01756D.

Volume 19
Number 1
7 January 2017
Pages 1-896

PCCP
Physical Chemistry Chemical Physics
rsc.li/pccp

ISSN 1463-9076

PAPER
H.-P. Loock *et al.*
Determination of the thermal, oxidative and photochemical degradation rates of scintillator liquid by fluorescence EEM spectroscopy

ROYAL SOCIETY OF CHEMISTRY

ROYAL SOCIETY
OF CHEMISTRY

rsc.li/pccp

View Article Online
DOI: 10.1039/D5CP01756D

ARTICLE

Received 00th January 20xx,
Accepted 00th January 20xx

DOI: 10.1039/x0xx00000x

Theoretical Determination of Linear and nonlinear Optical Properties as well as Electric Anisotropies of Elements of Periodic Table: A Density Functional Theory Study

Mahnaz Jabbarzadeh Sani

Herein the static and dynamic polarizabilities of the elements of the Periodic Table H-Rn are computed with the density functional theory (DFT) method using the property-optimized basis sets of quadruple-ζ valence quality. To obtain insight into the shape of the electron charge distribution around the nucleus of an isolated atom, a model based on the polarizability anisotropy is presented. According to this model, the atoms with a non-zero orbital electron angular momentum and a non-vanishing electric anisotropy are assumed to be ellipsoids of rotation. It is found that the shape transition occurs when the spin multiplicity alters, accompanied by a change in the electron configuration and charge distribution around the nucleus of the free atoms. The all-electron relativistic calculations reveal that the atomic Au is a spheroid with a prolate deformation. The computations of the present paper provide the complete determination of the linear and non-linear (NLO) optical properties as well as the electric anisotropies of the elements of the Periodic Table and give new insight into the deformation of the electron charge distributions around the nuclei of the isolated atoms with respect to the spherical symmetry.

Introduction

Since the development of quantum mechanics, the calculation of the electric dipole polarizabilities of the atoms has been subject of much interest. This quantity is useful in the theoretical description of the ultraprecision atomic clocks, interatomic interactions, electron-atom scattering and optical properties of materials.[1-11] There have been numerous studies of the atomic polarizabilities and the anisotropies in the last several decades, including alkali[12-17] and alkaline earth[15,18] metals, p-block elements,[19-36] d-block transition metals,[18,37-43] f-block elements[24,39,44-57] and noble gases.[15,18,23,58] The atomic hyperpolarizabilities are still unknown and there have been only a few theoretical and experimental studies of the electronic static hyperpolarizabilities[22,23,59,60] and the frequency-dependent (hyper)polarizabilities[61-69] in the literature. Stevens and Bilingsley,[70] using the multiconfigurational self-consistent-field wave functions computed the static dipole polarizabilities for the ground state and some valence excited states of the first-row atoms. The use of the multiconfigurational framework allowed any state of the both degenerate and non-degenerate atoms to be considered, and also allowed for the explicit introduction of electron-correlation effects. Werner and Meyer,[71] employing the self-consistent-field and highly correlated wavefunctions calculated the static dipole polarizabilities and anisotropies for the ground states of the atoms Li through Ne. The importance of the relativistic effects in the calculation of static dipole polarizabilities of the alkaline-earth elements Ca, Sr, Ba and Ra, the group 12 atoms Zn, Cd and Hg, and the inert gases Kr, Xe and Rn has been investigated by Lam.[18] This author concluded that the relativistic effects do not play any significant role on the dipole polarizabilities of the inert gas atoms. Stiehler and Hinze[59] calculated the static electric dipole polarizabilities and hyperpolarizabilities for different states of the ground configuration of the atoms He through Kr at the restricted Hartree-Fock level using the finite perturbation method. There are few reports which quantitatively discuss the anisotropy of electron density distributions around atoms in molecules.[72-78] For example, Nyburg and Faerman[74] using the structural database determined the effective van der Waals shapes of N, O, S, Se, F, Cl, Br and I atoms bonded to a single carbon atom. The authors found that for O and N, the shapes are virtually spherical, however, for the remainder, shape is more or less spheroidal, always having smaller radius along the atom-to-carbon vector.

In this paper, a systematic study of the polarizabilities and polarizability anisotropies of the elements of the Periodic Table is presented. Furthermore, the static $\gamma_{||}(0;0,0,0)$, the dc-Kerr $\gamma_{||}(-\omega;\omega,0,0)$ and the electric field-induced second-harmonic generation $\gamma_{||}(-2\omega;\omega,\omega,0)$ second-order hyperpolarizabilities for the elements H-Rn (except lanthanides) are reported. In the following sections, first the underlying theory and the details of the computational procedure is briefly outlined. Next, the results of the computed static and dynamic

---

*Chemistry Department, College of Science, Shiraz University, 7146713565 Shiraz Iran. Email: mjsani@shirazu.ac.ir

† Footnotes relating to the title and/or authors should appear here.

Supplementary Information available: [details of any supplementary information available should be included here]. See DOI: 10.1039/x0xx00000x

View Article Online
DOI: 10.1039/D5CP01756D

polarizabilities and second hyperpolarizabilities along with the electric anisotropies are presented. Then, to obtain insight into the shapes of the electron charge distributions around the nuclei of the isolated atoms, a model based on the polarizability anisotropy is proposed. Finally, the main findings of the present computations are summarized.

Theoretical background

The response of an atom to the external electric field E can be written as[79]

$$\mu_\lambda = \langle \Psi(E,t) \,|\, \hat{\mu}_\lambda \,|\, \Psi(E,t) \rangle$$
$$= \mu_{0\lambda} + \alpha_{\lambda\mu} E_\mu + \frac{1}{2!}\beta_{\lambda\mu\nu} E_\mu E_\nu + \frac{1}{3!}\gamma_{\lambda\mu\nu\eta} E_\mu E_\nu E_\eta + \ \ldots \qquad (2\text{-}1)$$

here the subscripts (λ, μ, etc.) relate to the Cartesian coordinates in atomic axis on which the external electric field is projected. μ is the dipole moment vector, and the expansion coefficients α, β and γ are the linear polarizability, the first- and the second-hyperpolarizability tensors of rank 2, 3 and 4, respectively. When a time-dependent electric field $E = E_0 + E_\omega \cos(\omega t)$ is applied, the expansion (2-1) is rewritten as[79]

$$\begin{aligned}
\mu_\lambda \ = \ & \mu_{0\lambda} \ + \ \alpha_{\lambda\mu}(0;0) E_{0\mu} \ + \ \alpha_{\lambda\mu}(-\omega;\omega) E_{\omega\mu} \cos(\omega t) \\
& + \tfrac{1}{2}\beta_{\lambda\mu\nu}(0;0,0) E_{0\mu} E_{0\nu} \ + \ \tfrac{1}{4}\beta_{\lambda\mu\nu}(0;\omega,-\omega) E_{\omega\mu} E_{\omega\nu} \\
& + \ \beta_{\lambda\mu\nu}(-\omega;0,\omega) E_{0\mu} E_{\omega\nu} \cos(\omega t) \\
& + \ \tfrac{1}{4}\beta_{\lambda\mu\nu}(-2\omega;\omega,\omega) E_{\omega\mu} E_{\omega\nu} \cos(2\omega t) \qquad (2\text{-}2) \\
& + \ \tfrac{1}{6}\gamma_{\lambda\mu\nu\eta}(0;0,0,0) E_{0\nu} E_{0\eta} \\
& + \ \tfrac{1}{2}\gamma_{\lambda\mu\nu\eta}(-\omega;\omega,0,0) E_{\omega\mu} E_{0\nu} E_{0\eta} \\
& + \ \tfrac{1}{4}\gamma_{\lambda\mu\nu\eta}(-2\omega;\omega,\omega,0) E_{\omega\mu} E_{\omega\nu} E_{0\eta} \cos(2\omega t) \ + \ \ldots
\end{aligned}$$

here, the frequency-dependent coefficients are denoted as follows: polarizability α(0;0) for static case; α(-ω;ω) for dynamic case; first-hyperpolarizability β(0;0,0) for static case; β(-ω;0,ω) for electrooptic Pockels effect (EOPE); β(-2ω;ω,ω) for second-harmonic generation (SHG); β(0;ω,-ω) for optical rectification (OR); second-hyperpolarizability $\gamma_{||}(0;0,0,0)$ for static case; $\gamma_{||}(-\omega;\omega,0,0)$ for optical Kerr effect (OKE); and $\gamma_{||}(-2\omega;\omega,\omega,0)$ for electric field-induced second-harmonic generation (EFISHG). For a centrosymmetric system, all odd-rank tensors vanish, so as a free atom possesses an inversion symmetry, the permanent dipole moment μ and the first-hyperpolarizability β are zero.[80-82] The dipole polarizability as a second-rank tensor, is a linear response property that is defined as the second derivative of the total energy with respect to a weak homogeneous external electric field.[83] The mean isotropic static polarizability is the average of the trace of the polarizability matrix[84,85]

$$\bar{\alpha} \ = \ \mathrm{Tr}\,(\alpha)\,/\,3 \ = \ (\alpha_{xx} + \alpha_{yy} + \alpha_{zz})\,/\,3 \qquad (2\text{-}3)$$

The symmetry axis of the isolated atom is exactly parallel to the external electric field, so that the polarizability is denoted by the parallel α_{zz} and the perpendicular $\alpha_{xx} = \alpha_{yy}$ components. The polarizability anisotropy also referred to as electric anisotropy is given by[84]

$$\alpha_2 \ = \ \frac{1}{\sqrt{2}}$$
$$\Big[\left(\alpha_{xx} - \alpha_{yy}\right)^2 + \left(\alpha_{yy} - \alpha_{zz}\right)^2 + (\alpha_{zz} - \alpha_{xx})^2 + \qquad 6\,\Big(\alpha_{xy}^2 + \alpha_{xz}^2$$
(2-4)

When the electric field direction coincides with the axis of symmetry of the isolated atom, the off-diagonal components of the polarizability matrix vanish and the components α_{xx} and α_{yy} become equal.[83] In this case, the anisotropic polarizability of equation (2-4) is rewritten as

$$\alpha_2 \ = \ \alpha_{zz} \ - \ \alpha_{xx} \qquad (2\text{-}5)$$

here α_{xx} and α_{zz} are the polarizabilities perpendicular and parallel to the symmetry axis of the isolated atom, respectively. In the case that all applied fields have parallel polarization, the measurable second-order hyperpolarizability is the scalar component of the tensor γ, given by the isotropic average[61,62,68,81]

$$\gamma_{||} \ = \ \frac{1}{15} \sum_{ij} (\gamma_{iijj} + \gamma_{ijij} + \gamma_{ijji}) \qquad (2\text{-}6)$$

here i, j = x, y, and z are the Cartesian components, and γ as a fourth-rank tensor, is a non-linear response property that is defined as the fourth derivative of the total energy with respect to a weak homogeneous external electric field. $\gamma_{||}$ (Eq. 2-6) is the parallel isotropic tensor component of the second-order hyperpolarizability.

Computational details

The static and dynamic polarizabilities and second-order hyperpolarizabilities of the elements of the Periodic Table H-Rn (except lanthanides) are computed with the density functional theory (DFT) method using the property- optimized diffuse augmented basis set of quadruple-ζ quality def2-QZVPPD.[86] The property-optimized basis sets use the relativistic effective core potentials for the elements Rb-Rn.[87] In order to know the best computational method, the dipole polarizabilities for the heavy elements including d-block transition metals Tl, Au, Ba, Hg, Po, p-block atoms At, Bi, Br, I, and noble gases Kr, Xe, Rn are calculated using different functionals and the def2-QZVPPD basis set and the results are summarized in Table S1. This Table contains the pure functionals BLYP, BP86, M06L, PBE, TPSS, the hybrid functionals B3LYP, B3PW, B1LYP, mPW1LYP, mPW1PW, TPSSh, and the long-range corrected functionals LC-BLYP, CAM-B3LYP. As Table S1 represents, the static dipole polarizabilities computed using the long-range corrected hybrid CAM-B3LYP[88] functional are in fairly close to those obtained from the conventional ab-initio methods. Especially, the polarizabilities calculated employing CAM-B3LYP functional agree at best with the most accurate CCSD(T) result of 36.06±0.54 a.u. for Au,[60,89] the Configuration Interaction (CI) values of 70.05 and 262.2 a.u. for Tl and Ba,[26,92,93] respectively, and the measured value of 27.82 for Xe. Furthermore, it has been revealed that the long-range correction method gives greatly improved results for the polarizabilities.[88] Hence, the optical properties for the elements H-Rn (except lanthanides) are computed using the long-range corrected hybrid CAM-B3LYP functional in conjunction with the quadruple-ζ quality def2-QZVPPD basis set. To know the effect of the long-range correction, computations using the Global hybrid functional B3LYP[100-102] are also performed. The hybrid functionals are considered a good compromise between the accuracy and the computational cost.[103,104] For the lanthanides, the polarizabilities are computed using the segmented contracted Gaussian basis set of quadruple-ζ quality def2-QZVPP[105] with the small-core Wood-Boring relativistic effective core potentials,[106] and the SARC-DKH-TZVPP basis set.[107-110] Since the Radon is the heaviest atom for which the property-optimized diffuse augmented basis sets are available, the polarizabilities and the polarizability anisotropies for the actinide series are computed using the segmented all-electron relativistically contracted SARC-DKH-TZVPP basis set.[107-110] For the elements H-Rn (except lanthanides), the frequency-dependent polarizabilities and the second-order hyperpolarizabilities are calculated in 1064.0 nm optical wavelength, that is a common wavelength for the optical dipole traps.[55] The relativistic contribution to the dipole polarizability has been found to be large for the atomic Au,[41] therefore all-electron relativistic density functional theory (DFT) calculations are also performed for the coinage metals with the all-electron relativistic DZP-DKH[111-113] basis set. The Douglas-Kroll no-pair method is expected to give results fairly close to those which would follow from the calculations based on the four-component Dirac-Coulomb equation,[114] hence the all-electron relativistic computations are carried out with the second-order Douglas-Kroll-Hess Hamiltonian.[115,116] The point-nucleus model is used for the all-electron relativistic calculations.[117] The molar volume, defined as the volume inside a contour of 0.001 electrons/bohr^3 density, is computed for the elements H-Rn (except lanthanides) employing the numerical Monte Carlo integration. To calculate the molar volumes in a more quantitative way, the keywords SCF=Tight and Volume=Tight are used. Furthermore, the volume calculations are repeated for each atom to increase the accuracies.[118,119] The calculations with the quadruple-ζ quality basis sets are performed using the Gaussian 09 program suite[120] and the all-electron relativistic computations are carried out with the ORCA (version 4.2.1) quantum chemistry program package.[121] The GaussView (version 6.0.16)[122] and the Multiwfn software pack (version 3.7)[123] are used to visualize the results of the all-electron relativistic density functional theory (DFT) calculations. The natural population analysis is carried out using the NBO (version 3.0) program within the Gaussian 09 package.[124]

Results and discussion

Isotropic static polarizabilities

The computed polarizability components α_{xx}, α_{yy} and α_{zz} as well as the mean isotropic static polarizabilities for the ground state of the elements of the Periodic Table H-Rn (except lanthanides) are summarized in Tables S2 and S3. As these Tables illustrate, across rows of the Periodic Table, the mean isotropic static polarizabilities range from the hundreds for the alkali metal atoms down to a few for noble gas atoms. Furthermore, the isotropic polarizabilities increase as the atomic number increases within a given group of the Periodic Table. However, as can be seen in Table S3, at the CAM-B3LYP/def2-QZVPPD level, the mean polarizability for the sodium $\bar{\alpha}$ = 146.21 a.u. is lower than the corresponding value for the lithium $\bar{\alpha}$ = 146.49 a.u. All-electron relativistic calculations at the DKH2-CAM-B3LYP/ANO-RCC-QZP level are also performed for the Li and Na, resulting in the polarizability values of 147.20 and 142.14 a.u., respectively, in agreement with the results obtained with the CAM-B3LYP/def2-QZVPPD level of theory. Within the framework of relativistic many-body theory, Johnson et al.[125] computed the ground-state polarizability of the Li and obtained value of 164.08 a.u. for this atom. Puchalski et al.[126] employing the relativistic and quantum electrodynamics corrections obtained value of 164.074(5) a.u. for the ground-state electronic dipole polarizability of Li. Using the relativistic ab initio methods, Derevianko et al.[127] reported the value of 162.6±0.3 a.u. for the polarizability of Na. It has been found that the measured mean polarizability for the sodium (162.7±0.5[128]) is also less than the corresponding value for lithium (164.2±1.1[129]). The reason is that the effective nuclear charge on the valence electron in lithium is smaller, resulting in more distributed electron cloud and higher polarizability for this atom. This indicates that the CAM-B3LYP/def2-QZVPPD level of theory produces a picture of the trend quite similar to those of the available theoretical and experimental polarizabilities for the Li and Na. It has been revealed that the incorrect long-range exchange interaction delivered by the conventional DFT exchange functionals lead to the underestimation of the 4s-3d interaction energies of the first-row transition metals and overestimation of the longitudinal polarizabilities of the π-conjugated polyenes.[88] The CAM-B3LYP functional combines the hybrid qualities of B3LYP and the long-range correction presented by Tawada et al.[130] It is presumed that this long-range correction for the exchange functionals of the density-functional-theory is responsible for the correct long-range orbital-orbital interaction and excitation energies and the improved electric dipole polarizabilities.[130,131] It is also noticed that the computed isotropic static polarizabilities show a reversal of trend for the groups 4 through 12 on going from the fifth to the sixth period. This is because the relativistic effects become significant as early as the 3d transition metals and they become more significant in the post-3d elements.[132,133] Especially, the relativistic contraction and stabilization of the orbitals of low angular momentum (ns) has considerable contribution to the computed polarizabilities. The transition metal atoms are characterized by the specific electronic structures due to a d-orbital collapse.[37] From Tables S2 and S3, the computed mean polarizability for the palladium is small values of 24.16 and 25.00 a.u. at the CAM-B3LYP/def2-QZVPPD and the B3LYP/def2-QZVPPD levels, respectively. The palladium atom is the only known atom in its ground electronic state not to have at least one electron in the outer-shell ns or np orbitals, so that the valence ground state electron configuration for the atomic palladium is closed-shell 4d^{10}, differing from all the other group 10 members which are open-shells ((n-1)d^{9}ns^1; n=4,6). Nagle et al.[43] also reported a small value of 26.14(10) a.u. for the mean polarizability of atomic palladium, that is in very good agreement with the results of the present calculations. Furthermore, as Tables S2 and S3 represent, the gallium atom apart from the increasing importance of the relativity, possesses nearly small mean polarizability values of 54.59 and 58.25 a.u. at the CAM-B3LYP/def2-QZVPPD and B3LYP/def2-QZVPPD levels, respectively; that are lower than the corresponding values for the aluminium atom. The reason lies in the higher effective nuclear charge experienced by an outer-electron in Ga, resulting in more compact valence shell and a reduced polarizability.

Anisotropic polarizabilities

The polarizability anisotropies of the elements of the Periodic Table H-Rn (except lanthanides) computed at the CAM-B3LYP/def2-QZVPPD and B3LYP/def2-QZVPPD levels of theory are summarized in Table S4. The main source of the polarizability anisotropy for the isolated atom is the orbital electronic angular momentum, i.e. the anisotropy is non-vanishing for the atoms with a non-zero orbital angular momentum $L\neq0$.[19] As Table S4 represents, since the ground state of the alkali and alkaline earth meals together with the closed-shell inert gases is an S-state (^{1}S, L=0), the polarizability anisotropy is zero for these elements of the Periodic Table. Furthermore, as in the limit of the LS-coupling, the ground state of a half-filled shell is an S-state, so the electric anisotropy for the group 15 elements of the Periodic Table also vanishes. In fact, the anisotropy is exactly zero for the S-state atoms, positive for the group 13 and 16 elements and negative for the elements in groups 14 and 17. As equation (2-5) illustrates, when the electron charge distribution oriented in the z-direction is more diffuse and thus more polarizable, a positive polarizability anisotropy is predicted. On the other hand, when the charge distribution in the xy plane is more diffuse and thus more polarizable than the z-direction, a negative polarizability anisotropy is obtained. As can be seen in Table S4, the polarizability anisotropy is the largest when the first p electron is added (group 13) and becomes smaller for the successive states as the valence shell fills. Therefore, for the first-row elements, the anisotropy for the open-shell boron atom is the largest, i.e. 5.907 and 6.653 a.u. at the CAM-B3LYP/def2-QZVPPD and B3LYP/def2-QZVPPD levels, respectively. Furthermore, the ^{2}P ground state of the thallium exhibits the largest atomic polarizability anisotropy values of 58.113 and 69.035 a.u. at the CAM-B3LYP/def2-QZVPPD and B3LYP/def2-QZVPPD levels, respectively. Using the configuration interaction (CI) calculations in the spin-free Dirac formalism, Fleig[26] obtained the value of 57.023 a.u. for the electric anisotropy of the thallium atom, that is in good agreement with the corresponding value of 58.113 a.u. computed at the CAM-B3LYP/def2-QZVPPD level of theory. In the case of the transition metal atoms (groups 3-12), the d-shell is unfilled, so a large anisotropy is expected for these elements of the Periodic Table; however, since the outer s-electrons screen the d-shell that is the only source of the anisotropy, small polarizability anisotropies are predicted for these elements.[44] In fact, the presence of the outer s-shell makes these atoms behave like an S-state atom, even though they carry a large internal angular momentum.[134] It has been found that removal of the outer electrons from the 4s orbital exposes the 3d orbitals a substantial overlap with the 1s orbital of the He atom which leads to the strongly anisotropic interaction.[135] So far, the polarizabilities and polarizability anisotropies have been described for the static fields. Tables S5 and S6 summarize the frequency-dependent polarizabilities and polarizability anisotropies computed at the wavelength of 1064.0 nm. As Tables S2-S6 represent, the numerical values of the mean isotropic static polarizability increase when the atom is immersed in an alternating electromagnetic field. For the S-state atoms, the both static and the frequency-dependent electric anisotropies are zero, indicating that the alternating electromagnetic field does not alter the sphericity of an isolated atom. Furthermore, except for the Ru and Mn, an increase in the magnitude of the anisotropies of the atoms with the non-zero orbital electronic angular momentum ($L\neq0$) is observed at the wavelength of 1064.0 nm. Employing the relativistic coupled-cluster method, Lesiuk and Jeziorski[69] reported the values of 11.0775(19) and 11.22445(11) a.u. for the static and frequency-dependent dipole polarizabilities of the argon, repectively, (λ=632.9908(2) nm) exhibiting an increase in the dipole polarizability of this atom with the frequency, that is in agreement with the results obtained in the present computations (Tables S2, S3, S5 and S6). Tables S7 and S8 contain the static $\gamma_{\parallel}(0;0,0,0)$, the dc-Kerr $\gamma_{\parallel}(-\omega;\omega,0,0)$, and the electric field-induced second-harmonic generation $\gamma_{\parallel}(-2\omega;\omega,\omega,0)$ second-order hyperpolarizabilities for the elements of Periodic Table H-Rn (except lanthanides) calculated with the density functional theory (DFT) method and the quadruple-ζ quality def2-QZVPPD basis set, in the wavelength λ = 1064.0 nm. Table S9 summarizes the static and the frequency-dependent hyperpolarizabilities for the lanthanides computed using the def2-QZVPP basis set. The reason for the negative sign of the second-order hyperpolarizabilities for the centrosymmetric atoms is that the virtual excitations between the ground and the excited states are stronger than the transitions between the excited states.[136] As can be seen in Table S7, the static and the dynamic second-order hyperpolarizabilities increase (decrease) as the atomic number increases within the groups 2, 15 and 18 (4,6-8,11,12), so that the trends in the second-order hyperpolarizabilities for the elements of the Periodic Table is dependent on the relativistic effects as well as the electronic states and spin multiplicities. Especially, the spin-multiplicity may have considerable effect on the trends of the static and dynamic second-order hyperpolarizabilities. For instance, at the CAM-B3LYP/def2-QZVPPD level, the computed second-order hyperpolarizabilities for the quartet vanadium display the trend of increasing magnitude from static to Kerr-effect to electric field-induced second-harmonic generation, i.e. $|\gamma(0;0,0,0)| = 7.65\times10^5$ a.u. $< |\gamma(-\omega;\omega,0,0)| = 7.74\times10^5$ a.u. $< |\gamma(-2\omega;\omega,\omega,0)| = 1.55\times10^6$ a.u.; whereas a reversal of the trend in the magnitudes of the second hyperpolarizabilities for the sextet vanadium is observed $|\gamma(0;0,0,0)| = 4.51\times10^6$ a.u. $> |\gamma(-\omega;\omega,0,0)| = 2.88\times10^6$ a.u. $> |\gamma(-2\omega;\omega,\omega,0)| = 5.08\times10^5$ a.u.. Furthermore, the second-order hyperpolarizabilities of the lithium and sodium atoms display the same trend as the mean dipole polarizabilities, i.e. the sodium atom has lower static and dynamic second-order hyperpolarizabilities as compared with the lithium, that is a result of the smaller effective nuclear charge on the valence electrons and the more distributed electron cloud around the nucleus of the Li atom. Using the multiconfigurational time-dependent Hartree-Fock method, Jaszuński and Yeager[63] obtained the value of 86.5 a.u. for the static second-order hyperpolarizability of the neon. The computed static second-order hyperpolarizability values of 80.2 and 83.1 a.u. at the CAM-B3LYP/def2-QZVPPD and B3LYP/def2-QZVPPD levels, respectively; are in good agreement with the corresponding $\gamma_{\parallel}(0;0,0,0)$ value of 86.5 a.u. reported by Jaszuński and Yeager,[63] and also with the experimental value of 75 a.u. $< \gamma_{\parallel} <$ 93 a.u.[64] for Ne. At the CCSD/t-aug-cc-pV5Z level, Hättig and Jørgensen[61] obtained the value of 1237 a.u. for the second-harmonic generation $\gamma_{\parallel}(-2\omega;\omega,\omega,0)$ of the argon atom (λ = 1064.0 nm) that is in agreement with the corresponding values of 925 and 1020 a.u. computed at the CAM-

B3LYP/def2-QZVPPD and B3LYP/def2-QZVPPD levels, respectively. These authors reported the value of 889.7 a.u. for the static hyperpolarizability of Ar at the HF/d-aug-cc-pVQZ level, that is also in agreement with the corresponding values of 848 and 917 a.u. computed at the CAM-B3LYP/def2-QZVPPD and B3LYP/def2-QZVPPD levels, respectively. Employing CCSD/t-aug-cc-pV5Z method, Høst et al.[62] reported the value of 2.83×10^3 a.u. for the second-harmonic generation of Krypton in good agreement with the corresponding values of 2.25×10^3 and 2.01×10^3 a.u. at the CAM-B3LYP/def2-QZVPPD and B3LYP/def2-QZVPPD levels, respectively. The reasonable agreement between the computed second-order hyperpolarizabilities at the CAM-B3LYP/def2-QZVPPD and B3LYP/def2-QZVPPD levels with the other theoretical and experimental values may indicate that the theoretical methods employed here are adequately reliable for the calculation of the second-order hyperpolarizabilities of the elements of the Periodic Table.

Polarizabilities and polarizability anisotropies of the f-block elements

The computed polarizabilities and polarizability anisotropies of the lanthanide atoms are summarized in Table S10. From this Table, it is noted that if atoms with a partly filled d-shell are ignored, then there is a steady decrease of the mean isotropic static polarizabilities with the increasing atomic number. In the case of the open-shell lanthanides, the outer spherical $6s^2$ electronic shell screens the 4f sub-shell and suppresses the resulting polarizability anisotropies. As Table S10 represents, the values of the electric anisotropies are controlled largely by the $5d^1$ sub-shell, so that the lanthanum, gadolinium and lutetium exhibit relatively high magnitudes of 11.720, 7.569 and 23.699 a.u. for the electric anisotropies, respectively. The experimental polarizability anisotropies for the lanthanum and gadolinium are 10.45 and 7.87a.u., respectively,[39,56] that are in very good agreement with the computed anisotropy values of 11.720 and 7.569 a.u. for these atoms. Employing the time-dependent density functional theory (DFT), Dalgarno et al.[50] calculated the electric anisotropies for the rare-earth-metal atoms and obtained the values of 10.12 and 6.27 a.u. for the lanthanum and gadolinium, respectively. The results of these authors are in agreement with the corresponding computed values of 11.720 and 7.569 a.u. for the La and Gd, respectively. Within the actinide series from the actinium to the lawrencium, all the isotopes are radioactive.[137] The polarizabilities and polarizability anisotropies for the actinide series computed at the all-electron relativistic DKH2-B3LYP/SARC-DKH-TZVPP level are summarized in Table S11. As this Table illustrates, the actinium without a 5f-electron $[\mathrm{Rn}]6d^17s^2$, the curium with a half-filled 5f-shell $[\mathrm{Rn}]5f^76d^17s^2$, and the lawrencium with a completely-filled 5f-shell $[\mathrm{Rn}]5f^{14}6d^17s^2$ exhibit high magnitudes of the 9.325, 11.093 and 60.649 a.u. for the anisotropies of these elements, respectively. In the case of the remaining open-shell actinides, the outer $7s^2$ electronic shell screens the inner 5f-shell and suppresses the resulting electric anisotropies. Furthermore, as can be seen in Table S11, the computed mean polarizability for the Lr atom is 115.70 a.u. The relatively high mean isotropic static polarizability value of 115.70 a.u. for lawrencium compared with the corresponding value for the nobelium (91.934 a.u.) is attributed to the screening effects of the completely-filled 4f and 5f-shells, resulting in a decrease in the binding energy of the $6d^1$ shell and the increased mean polarizability for the Lr atom (Table S11). In fact, the polarizability is mostly dependent on the valence electrons, i.e. the outer part of the electron cloud is the most crucial in determining the polarizability.[138]

Shape of the electron charge distribution around the nuclei of isolated atoms

In this section, a simple model is presented to determine the shape of the electron charge distribution around the nucleus of the isolated atom. The electric anisotropy of a free atom can be considered as a measure of the deformation of the electron charge distribution with respect to the spherical symmetry; hence, the computation of the anisotropy of the ground-state atom might give information on the shape of the electron charge distribution around the nuclei of the elements of the Periodic Table. In this model, the electron charge distribution of the free atom is approximated by a uniform ellipsoid of rotation. Figure S1 represents the intersections of a sphere and the ellipsoids of rotation with the xz plane. As this Figure illustrates, because of the non-zero orbital electronic angular momentum, the hypothetical circle with mean radius R_s deforms to the ellipsoids with semimajor axis R_a and the semiminor axis R_b. It is assumed that the deformation is such a way that the perimeter of the circle to be remained equal to the perimeter of the ellipse $\pi(R_a + R_b)$.[139,140] It then follows that

$$R_a = 2R_s - R_b \qquad (3\text{-}1)$$

When the semimajor axis and the semiminor axis of the ellipse are approximately equal ($R_a \approx R_b$), the radius of the circle can be approximated by the arithmetic mean of the two semi-axes of the ellipse, i. e. $R_s = (R_a + R_b)/2$. In this case, the perimeter of the circle equals the perimeter of the ellipse.[141] As it will be mentioned in this section, the semimajor and the semiminor axes of the non-spherical elements of the Periodic Table are approximately the same; hence the aforementioned assumption is justified; and the formula used for the perimeter of an ellipse is physically appropriate for the determination of the shape of the electron charge distribution around the nucleus of the isolated atom.[142,143] In the Gaussian system of the electrical units, the dipole polarizability has the dimensions of the volume,[142] so the key to solving for the semiminor axis R_b is the assumption that the cube root of the electric anisotropy α_2 is proportional to 2C (Fig. S1), or equivalently

$$\sqrt[3]{\alpha_2} = \zeta 2C \qquad (3\text{-}2)$$

here ζ is the constant of proportionality,[144] that for the simplicity equals unity; however, as the dipole polarizability describes the second-order response of an isolated atom to the external field at the properly taken F→0 limit, i.e. $\alpha_{ij} = \left(\frac{\partial^2 E}{\partial F_i \partial F_j}\right)_{F\to 0}$,[26] then the assumption $\zeta = 1$ is well justified. Plugging equations (3-1) and (3-2) into the Pythagorean relation for an ellipse[145] $C^2 = R_a^2 - R_b^2$ and then solving the resulting equation, yields

View Article Online
DOI: 10.1039/D5CP01756D

$$R_b = R_s - \frac{\sqrt[3]{\alpha_2^2}}{(16\, R_s)} \qquad (3\text{-}3)$$

here, R_a and R_b are the semimajor and the semiminor axes; the mean radii R_s are derived using the computed molar volumes; and the electric anisotropy α_2 is in the unit of A°^{3}. Equations (3-1) and (3-3) are used for the calculation of the semimajor axis R_a and the semiminor axis R_b and the eccentricities[145,146] for the elements H-Rn and the results are listed in Tables S12 and S13. Figure 1 illustrates the electron charge distribution around the nucleus of an isolated atom; so that the symmetry axis for the charge distribution is the direction of the parallel component of the static polarizability α_{zz}. From this Figure, the electric anisotropy vanishes when the isolated atom is spherically symmetric. In the case of a prolate, the polarizability anisotropy is positive, whereas for an oblate, the anisotropy is negative (equation 2-5). As can be seen in Tables S4 and 11, the S-state atoms (^{1}S, L=0) with zero electric anisotropies are spherically symmetric ($R_a = R_b$; ε=0), the elements in groups 14 and 17 (L≠0; $\alpha_2<0$) are spheroids with oblate deformation, while the group 13 and 16 elements (L≠0; $\alpha_2>0$) are prolate ellipsoids of rotation. Furthermore, the thallium atom with the ^{2}P ground-state exhibits the largest eccentricity value of ε=0.42, and the difference between the semimajor and the semiminor axis lengths for this atom is only 0.24 A°. In addition, the electron configuration and charge distribution around the nucleus of the atom can be substantially changed upon varying its spin multiplicity. For instance, at the CAM-B3LYP/def2-QZVPPD level, the triplet tungsten is a spheroid with oblate deformation (^{3}D; α_2 = -0.258 a.u.), while the quintet W atom is a prolate (^{5}D; α_2 = +5.27 a.u.). When this atom is in the septet state, the polarizability anisotropy vanishes, resulting in a spherically symmetric electron charge distribution around the nucleus of the atom (^{7}S; α_2 = 0). The all-electron relativistic computations are also performed at the all-electron relativistic DKH2-PBE/DZP-DKH level for the triplet, quintet and septet tungsten. At this level of theory, the quintet and septet W are also prolate (^{5}D, α_2 = +4.19 a.u.) and spherically symmetric (^{7}S, α_2 = 0), respectively. For the triplet tungsten, the triaxial ellipsoidal deformation ($\alpha_{xx} \neq \alpha_{yy} \neq \alpha_{zz}$; $|\alpha_2|$ = 1.46 a.u. (Eq. 2-4)) is predicted at the all-electron relativistic DKH2-PBE/DZP-DKH level. Laun and Corliss[147] have measured the first spectrum of tungsten (WI) in the region between 2000 and 10500 A° and identified the quintet W (^{5}D, $4d^4$ $6s^2$) as the ground-state, in agreement with the present computations at the all-electron relativistic DKH2-PBE/DZP-DKH level (Fig. 2). The observed spectrum of WI by Laun and Corliss[147] exhibits different triplet states having relatively small energy separations (^{3}P, ^{3}H, ^{3}G, ^{3}F and ^{3}D), indicating a relatively complex triplet state for the neutral tungsten. This may result in the triaxial ellipsoidal deformation ($\alpha_{xx} \neq \alpha_{yy} \neq \alpha_{zz}$) for the charge distribution around the nucleus of the triplet W at the all-electron relativistic DKH2-PBE/DZP-DKH level. Based on aforementioned results, it is concluded that the spin multiplicity can impose a non-negligible effect on the shapes of the charge distributions of the free atoms, so that the shape transition can occur when the spin multiplicity alters. In other words, the change of the spin multiplicity may exhibit prolate-oblate and spherical-deformed competition for the electron charge distribution around the nucleus of the isolate atom. Furthermore, one of the consequences of the electric anisotropies is the orientational interaction and adsorption of a non-spherical atom at the charged surfaces, so that the anisotropic atoms can align differently perpendicular or parallel with a charged surface.

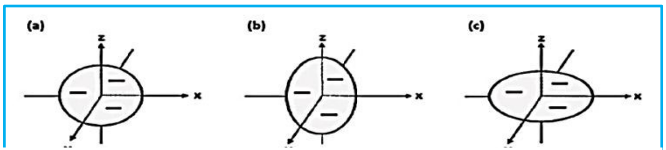

Fig. 1 . Charge distribution in an isolated atom. (a) Atom is spherically symmetric, then the polarizability anisotropy vanishes. (b) Atom is a "prolate" ellipsoid; the polarizability anisotropy is positive. (c) Atom is an "oblate" ellipsoid; the polarizability anisotropy is negative.

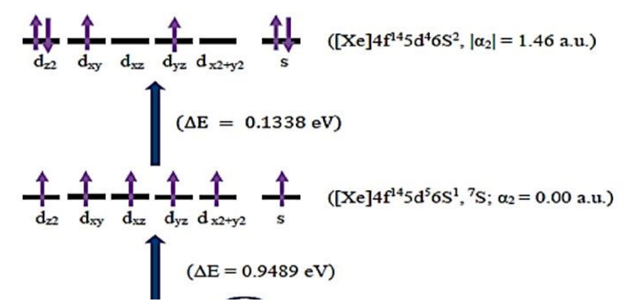

Fig. 2. Electron configurations, electronic states and electric anisotropies for the triplet, quintet and septet W atom computed at the all-electron relativistic DKH2-PBE/DZP-DKH level. The d-orbital populations for the triplet state are: $n(d_{xy})$ =1, $n(d_{yz})$ =1, $n(d_{x2+y2})$=0.84 and $n(d_{z2})$=1.16. According to Laun and Corliss[147], ^{3}P is the lowest energy triplet state.

As is well known, the relativistic effects are important in the study of the heavy elements.[148] Especially, the relativistic contraction and stabilization of the ns valence shell (n=4-6) undergoes a local maximum at the coinage metals.[149,150] Furthermore, the available theoretical computations on the noble metal clusters have revealed that the copper and silver clusters are planar up to six atoms,[151] whereas the gold clusters may remain planar up to 11[151] or even 15[152] atoms. This indicates that the ground-state electron configuration of the atomic gold is different from those of the copper and silver. Here, the all-electron relativistic and non-relativistic computations at the DKH2-B3LYP/DZP-DKH and B3LYP/DZP levels are performed for the atomic Cu, Ag and Au and the surfaces of the electrostatic potential (ESP) and the electron spin density along with the ground-state electron configurations and the electric anisotropies are represented in Fig. 3. As can be seen in this Figure, the non-relativistic surfaces of the electrostatic potential (ESP) and the electron spin density for the copper, silver and gold are spherically symmetric, indicating a zero polarizability anisotropy for these atoms. However, the all-electron relativistic computations reveal that unlike the Cu and Ag, there is a non-spherical electron charge distribution around the nucleus of the gold, resulting in a non-zero anisotropy value of α_2 = 1.648 a.u. for this atom. Furthermore, the shaded surface map with projection of the electron spin density for the atomic Au computed at the all-electron relativistic DKH2-B3LYP/DZP-DKH level of theory is presented in Fig. 4. As this Figure illustrates, the core region represents a spherically-symmetric electron spin density; whereas the valence shell exhibits asymmetric electron spin density for the atomic

View Article Online
DOI: 10.1039/D5CP01756D

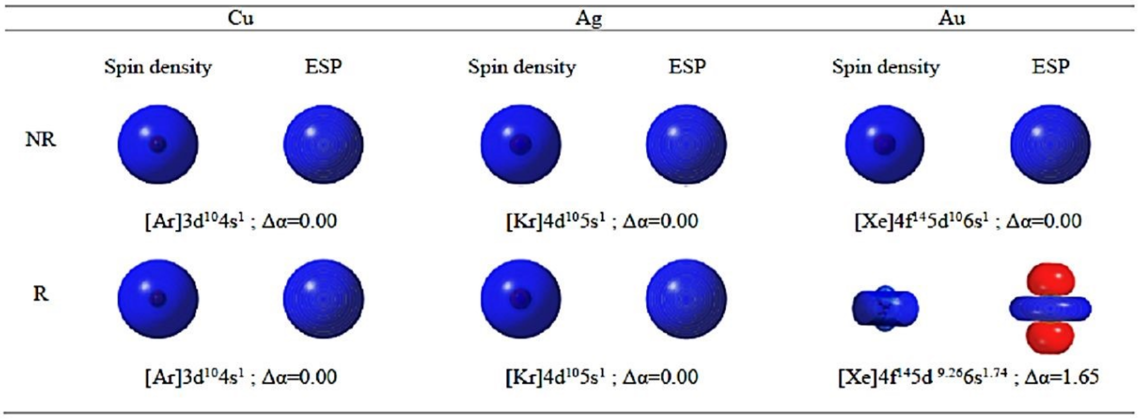

Fig. 3. Surfaces of the electrostatic potential (ESP) and electron spin density together with the ground state electron configurations and the electric anisotropies (α_2/a.u.) calculated at the all-electron non-relativistic (NR) and relativistic (R) B3LYP/DZP and DKH2-B3LYP/DZP-DKH levels of theory, respectively; for the atomic Cu, Ag and Au. Blue and red regions correspond to positive and negative electron spin density/electrostatic potential values, respectively.

Au. Fig. 5 depicts the all-electron non-relativistic and relativistic energy levels for the Au computed at the B3LYP/DZP and DKH2-B3LYP/DZP-DKH levels, respectively. As this Fig. illustrates, the relativistic effects result in the splitting of the α-spin and the β-spin d-orbitals, and more importantly, the relativistic effects contract and destabilize the low-angular momentum 6s orbital, so that the shrinkage is more enhanced in the case of the β-spin 6s orbital, allowing for the sd-hybridization of the β-spin 6s and $5d_{z2}$ orbitals.

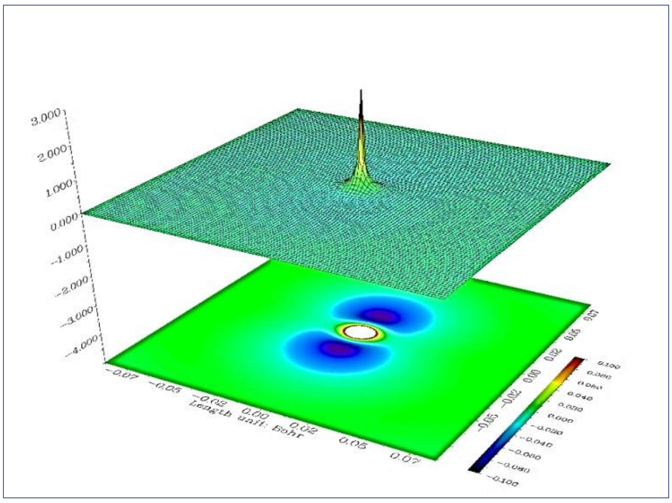

Fig. 4. Shaded surface map with projection effect of electron spin density of atomic Au computed at the all-electron relativistic DKH2-B3LYP/DZP-DKH level of theory.

are sd-hybridized. Furthermore, the natural population analysis along with the Mulliken and the Löwdin population analyses[121] reveal that the all-electron relativistic ground-state electron configuration for the atomic Au is $[Xe]4f^{14}5d^{9.26}6s^{1.74}$, indicating that the ground-state of this atom is nearly ^2D state. The Mulliken and the Löwdin population analyses[121] using the fully variational spin-orbit coupled CASSCF[121,153] level of theory are also carried out for the atomic gold with the second-order Douglas-Kroll-Hess Hamiltonian and the spin-orbit mean-field (SOMF) approach.[154,155] The active space includes one s-, five d-, and three p- orbitals, resulting in 11 electrons distributed over 9 orbitals. The calculated ground-configuration at the fully variational spin-orbit coupled CASSCF treatment, i.e. $[Xe]4f^{14}5d^9 6s^2$; $^2D_{5/2}$ is in agreement with the ground configuration computed using the all-electron relativistic density functional theory (DFT) method. The results indicate that the non-S state with a non-zero orbital electron angular momentum is responsible for the non-spherical electron charge distribution around the nucleus of the atomic gold. At the all-electron relativistic DKH2-B3LYP/DZP-DKH level, the polarizabilities of the atomic Au in the x and y directions are $\alpha_{xx} = \alpha_{yy} = 32.178$ a.u. and differ from the one in the z direction $\alpha_{zz} = 33.826$ a.u., resulting in a positive polarizability anisotropy value of $\alpha_2 = 1.648$ a.u., i.e. the atomic gold is a spheroid with a prolate deformation (R_a=2.2359 A°, R_b=2.2139 A°, ε=0.1399). Furthermore, as Table S14 illustrates, the all-electron relativistic electric anisotropies for the atomic Au computed with the different functionals are also positive; for instance, the all-electron relativistic DKH2-CAM-B3LYP/DZP-DKH, DKH2-TPSSh/DZP-DKH and

View Article Online
DOI: 10.1039/D5CP01756D

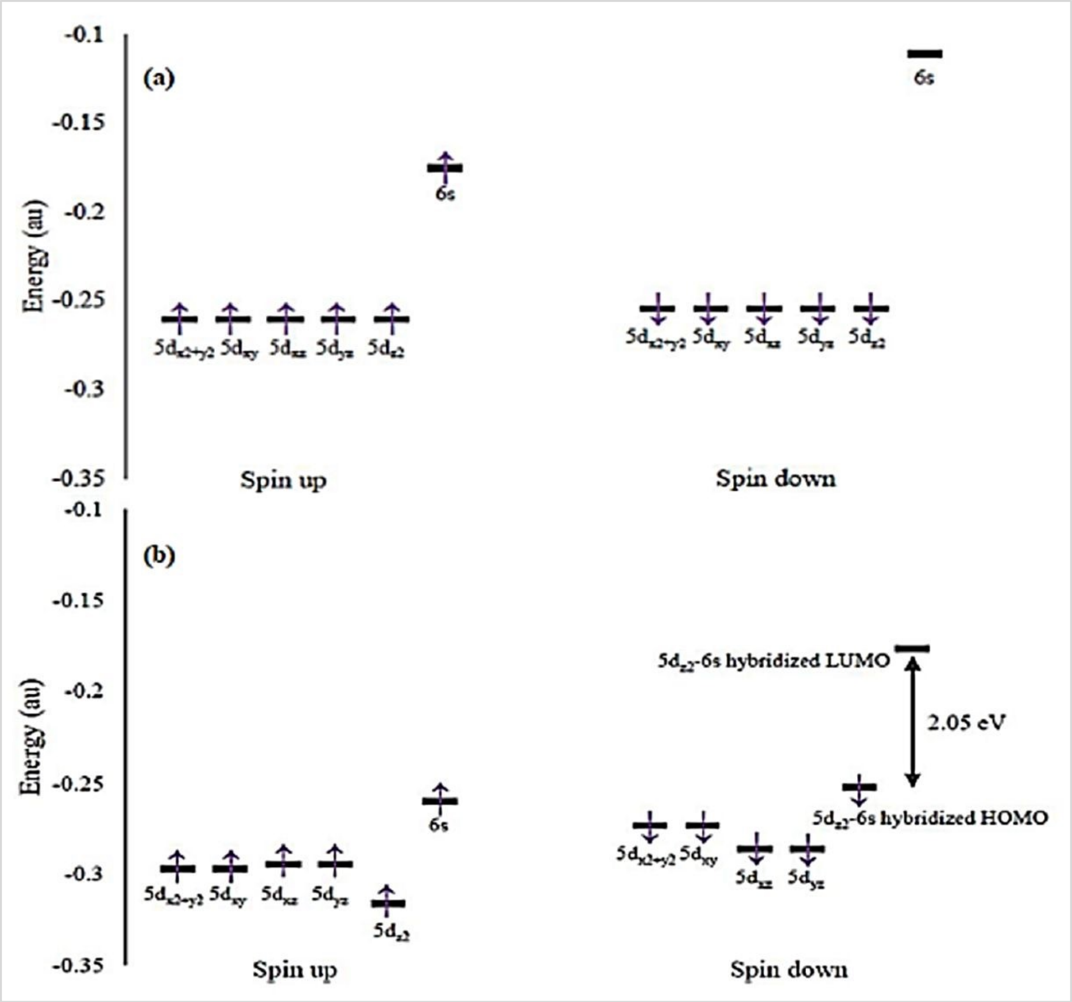

Fig. 5. Energy level diagram for a single gold atom computed at the (a) all-electron non-relativistic B3LYP/DZP and (b) all-electron relativistic DKH2-B3LYP/DZP-DKH levels.

DKH2-BHandHLYP/DZP-DKH levels predict positive anisotropy values of +1.777, +1.916 and +1.906 a.u., respectively; confirming that the relativistic Au atom is a prolate ellipsoid. It has been revealed that the nucleus of the ^{197}Au with a positive nuclear quadruple moment +0.521(7) b (nuclear spin = 3/2) is also a prolate when the symmetry axis of the nuclear charge distribution is the direction of the nuclear spin vector. (The quadruple moments are in units of barns; 1 b = 10^{-28} m^2). [156,157,158, 159] Furthermore, it has been found that the onset of the optical absorption for the gold is nearly 2 eV.[148] As can be seen in Fig. 5b, the energy splitting between the β-spin highest-occupied molecular orbital (HOMO) and the lowest-unoccupied molecular orbital (LUMO) of the atomic Au is 2.05 eV, indicating that the onset of the optical absorption in the middle of the visible is well reproduced by the present computations.

Conclusions

In the present paper, the static polarizabilities and polarizability anisotropies of the elements of the Periodic Table H-Rn are computed with the density functional theory (DFT) and the property-optimized basis sets of quadruple-ζ valence quality. The frequency-dependent dipole polarizabilities, second hyperpolarizabilities and electric anisotropies for the elements H-Rn (except lanthanides) are calculated at the wavelength of 1064.0 nm. It is found that the electric anisotropies are zero for the S-state atoms, while the non-vanishing anisotropies are predicted for the isolated atoms with the non-zero orbital electronic angular momentum. In order to know the shapes of the electron charge distributions around the nuclei of the elements of the Periodic Table, a model based on the electric anisotropies is presented and the semimajor and the semiminor axes along with the

View Article Online
DOI: 10.1039/D5CP01756D

eccentricities for the spheroidal atoms with the non-vanishing anisotropies are computed. It is revealed that the elements in groups 14 and 17 are spheroids with oblate deformation, while the group 13 and 16 elements are prolate ellipsoids of rotation. It is also found that the shape transition occurs when the spin-multiplicity alters, accompanied by a change in the electron configuration and charge distribution around the nucleus of the isolated atom. Employing the all-electron relativistic calculations, it is found that the non-S state with a non-zero orbital electron angular momentum is responsible for the non-spherical electron charge distribution around the nucleus of the atomic gold. These calculations also reveal that the atomic Au is a spheroid with a prolate deformation. It is also found that the CAM-B3LYP/def2-QZVPPD level outperforms the B3LYP/def2-QZVPPD method by producing a picture of the trend quite similar to the available theoretical and experimental polarizabilities for the elements of the Periodic Table, indicating that the long-range correction is necessary to obtain reliable linear and non-linear optical (NLO) properties for the isolated atoms. The computations of the present research work provide the complete determination of the deformation of the electron charge distributions around the nuclei of the gas-phase atoms with respect to the spherical symmetry.

Data availability

The data supporting this article have been included as part of the ESI.

Author contributions

Conceptualization; theoretical calculations; investigation; methodology; writing–original draft; writing – review & editing.

Conflicts of interest

There are no conflicts to declare.

References

1 C. Wang, Y. Yao, H. Shi, H. Yu, L. Ma and Y. Jiang, *Appl. Phys. Lett.*, 2025, 126, 031101.

2 J. Dutta, B. Mukherjee and J. M. Hutson, *cond-mat.quant-gas*, 2025, arXiv:2501.03170.

3 M. Z. Walewski, M. D. Frye, O. Katz, M. Pinkas, R. Ozeri and M. Tomza, Sci. Adv., 2025, 11, eadr8256.

4 M. Rossi, K. Rossi, A. M. Lewis, M. Salanne and A. Grisafi, *J. Phys. Chem. Lett.*, 2025, 16, 2326-2332.

5 C. Lyu, C. H. Keitel and Z. Harman, *Commun. Phys.*, 2025, 8, 3.

6 Y. Duan, J. Wang, P. Cieplak and R. Luo, *J. Chem. Inf. Model.*, 2025, 65, 1428-1440.

7 I. Puljić, A. Cipriš, D. Aumiler, T. Ban and N. Šantić, *Phys. Rev. A*, 2025, 111, 032809.

8 M. Giordano, F. O. Alfano, F. P. D. Maio and A. D. Renzo, *Sci. Rep.*, 2025, 15, 3121.

9 M. H. Seo, J. Mun, S. B. Lee and J. H. Lee, *EPJ Quantum Technol.,* 2025, 12, 13.

10 D. S. Grün, S. J. M. White, A. Ortu, A. D. Carli, H. Edri, M. Lepers, M. J. Mark and F. Ferlaino, *physics.atom-ph*, 2024, arXiv:2406.16146.

11 J. Klos, E. Tiesinga and S. Kotochigova, *Sci Rep.,* 2024, 14, 9267.

12 Z. L. Nie, J. Wang, C. L. Hu, Y. R. Sun, C. F. Cheng, Y. Tan and S. M. Hu, *Phys. Rev. A*, 2025, 111, 012801.

13 U. Kaldor, *J. Phys. B: At. Mol. Phys.,* 1973, 6, 71-75.

14 M. D. Gregoire, I. Hromada, W. F. Holmgren, R. Trubko and A. D. Cronin, *Phys. Rev. A,* 2015, 92, 052513.

15 J. P. Desclaux, L. Laaksonen and P. Pyykkö, *J. Phys. B: At. Mol. Phys.,* 1981, 14, 419-425.

16 A. Khadjavi, A. Lurio and W. Happer, *Phys. Rev.,* 1968, 167, 128-135.

17 C. Zhu, A. Dalgarno, S. G. Porsev and A. Derevianko, *Phys. Rev. A,* 2004, 70, 032722.

18 L. T. S. F. Lam, *J. Phys. B: At. Mol. Phys.,* 1981, 14, 3543-3549.

19 A. A. Buchachenko, *Proc. R. Soc. A,* 2011, 467, 1310-1328.

20 A. A. Buchachenko, *Russ. J. Phys. Chem. A,* 2010, 84, 2325–2333.

21 M. Medved, P. W. Fowler and J. M. Hutson, *Mol. Phys.,* 2000, 98, 453-463.

22 A. K. Das and A. J. Thakkar, *J. Phys. B: At. Mol. Opt. Phys.,* 1998, 31, 2215-2223.

23 C. Lupinetti and A. J. Thakkar, *J. Chem. Phys.,* 2005, 122, 044301.

24 N. J. Martin, P. G. H. Sandars and G. K. Woodgate, *Proc. Roy. Soc. A,* 1968, 305, 139-148.

25 T. Fleig and A. J. Sadlej, *Phys. Rev. A,* 2002, 65, 032506.

26 T. Fleig, *Phys. Rev. A,* 2005, 72, 052506.

27 T. P. Guella, T. M. Miller, B. Bederson, J. A. D. Stockdale and B. Jaduszliwer, *Phys. Rev. A,* 1984, 29, 2977.

28 J. D. Feichtner, M. E. Hoover and M. Mizushima, *Phys. Rev.*, 1965, 137, A702-A708.

29 P. Fuentealba, *Chem. Phys. Lett.,* 2004, 397, 459-461.

30 N. B. Vilas, B. Y. Wang, P. M. Rupasinghe, D. L. Maser, M. S. Safronova, U. I. Safronova and P. K. Majumder, *Phys. Rev. A,* 2018, 97, 022507.

31 M. S. Safronova and P. K. Majumder, *Phys. Rev. A,* 2013, 87, 042502.

32 C. Thierfelder, B. Assadollahzadeh, P. Schwerdtfeger, S. Schäfer and R. Schäfer, *Phys. Rev. A,* 2008, 78, 052506.

33 K. Andersson and A. J. Sadlej, *Phys. Rev. A,* 1992, 46, 2356-2362.

34 V. Pershina, A. Borschevsky, E. Eliav and U. Kaldor, *J. Chem. Phys.,* 2008, 128, 024707.

35 M. G. Kozlov, S. G. Porsev and W. R. Johnson, *Phys. Rev. A,* 2001, 64, 052107.

36 V. Pershina, A. Borschevsky, E. Eliav and U. Kaldor, *J. Phys. Chem. A,* 2008, 112, 13712-13716.

37 J. Kłos, *J. Chem. Phys.,* 2005, 123, 024308.

38 S. G. Porsev, D. Filin, C. Cheung and M. S. Safronova, *physics.atom-ph*, 2025, arXiv:2503.08855v1.

39 R. H. Rinkleff and F. Thorn, *Z. Phys. D,* 1994, 31, 31-36.

40 B. K. Sahoo and Y. M. Yu, *Phys. Rev. A,* 2018, 98, 012513.

41 P. Schwerdtfeger and G. A. Bowmaker, *J. Chem. Phys.,* 1994, 100, 4487-4497.

42 X. Chu and A. Dalgarno, *J. Chem. Phys.,* 2004, 121, 4083-4088.

43 P. Jerabek, P. Schwerdtfeger and J. K. Nagle, *Phys. Rev. A,* 2018, 98, 012508.

44 A. A. Buchachenko, M. M. Szczśniak and G. Chałasiński, *J. Chem. Phys.,* 124, 2006, 114301.

45 R. G. Rinkleff, A. Steudel and K. Zeiske, *Z. Phys. D – Atoms, Molecules and Clusters,* 1991, 18, 101-105.
46 R. H. Rinkleff and F. Thorn, *Z. Phys. D - Atoms, Molecules and Clusters,* 1994, 32, 173-177.
47 A. A. Golovizin, E. S. Kalganova, D. D. Sukachev, G. A. Vishnyakova, D. O. Tregubov, K. Y. Khabarova, V. N. Sorokin and N. N. Kolachevsky, *Quantum Electron.,* 2017, 47, 479-483.
48 J. H. Becher, S. Baier, K. Aikawa, M. Lepers, J. F. Wyart, O. Dulieu and F. Ferlaino, *Phys. Rev. A,* 2018, 97, 012509.
49 M. Lepers, J. F. Wyart and O. Dulieu, *Phys. Rev. A,* 2014, 89, 022505.
50 X. Chu, A. Dalgarno and G. C. Groenenboom, *Phys. Rev. A,* 2007, 75, 032723.
51 A. A. Buchachenko, G. Chałasiński and M. M. Szczęśniak, *Struct. Chem.,* 2007, 18, 769-772.
52 H. Li, J. F. Wyart, O. Dulieu and M. Lepers, *Phys. Rev. A,* 2017, 95, 062508. Erratum: *Phys. Rev. A,* 2018, 97, 029901.
53 H. Li, J. F. Wyart, O. Dulieu, S. Nascimbène and M. Lepers, *J. Phys. B: At. Mol. Opt. Phys.,* 2017, 50, 014005.
54 V. A. Dzuba, V. V. Flambaum and B. L. Lev, *Phys. Rev. A,* 2011, 83, 032502.
55 W. Kao, Y. Tang, N. Q. Burdick and B. L. Lev, *Opt. Express,* 2017, 25, 3411-3419.
56 R. H. Rinkleff, C. Ruhe and F. Thorn, *Z. Phys. D - Atoms, Molecules and Clusters,* 1993, 27, 39–43.
57 A. Müller, G. J. P. Deblonde, P. Ercius, S. E. Zeltmann, R. J. Abergel and A. M. Minor, *Nat. Commun.,* 2021, 12, 948.
58 M. Rérat and C. Pouchan, *Phys. Rev. A,* 1994, 49, 829-832.
59 J. Stiehler and J. Hinze, *J. Phys. B: At. Mol. Opt. Phys.,* 1995, 28, 4055-4071.
60 A. J. Thakkar and C. Lupinetti, *Theoretical approaches to the calculation of electric polarizability: Atoms, molecules and clusters in electric fields,* Imperial College Press, London, 2006, pp. 505–529.
61 C. Hättig and P. Jørgensen, *J. Chem. Phys.*, 1998, 109, 2762-2778.
62 S. Høst, P. Jørgensen, A. Köhn, F. Pawtowski, W. Klopper and C. Hättig, *J. Chem. Phys.*, 2005, 123, 094303.
63 M. Jaszuński and D. L. Yeager, *Phys. Rev. A*, 1989, 40, 1651.
64 D. P. Shelton and Z. Lu, *Phys. Rev. A*, 1988, 37, 3813.
65 D. P. Shelton, *Phys. Rev. A*, 1990, 42, 2578-2592.
66 S. J. A. van Gisbergen, J. G. Snijders and E. J. Baerends, *J. Chem. Phys*., 1998, 109, 10644-10656.
67 A. Banerjee and M. K. Harbola, *Physics.atom-Ph*, 2000, arXiv:Physics/0008139v.
68 D. P. Shelton and J. E. Rice, *Chem. Rev.*, 1994, 94, 3-29.
69 M. Lesiuk and B. Jeziorski, *Physics.Chem-ph*, 2023, arXiv:2301.12502v2.
70 W. J. Stevens and F. P. Billingsley, *Phys. Rev. A,* 1973, 8, 2236-2245.
71 H. J. Werner and W. Meyer, *Phys. Rev. A,* 1976, 13, 13-16.
72 S. Ikuta, *J. Mol. Struct. THEOCHEM,* 1990, 205, 191-201.
73 B. Bankiewicz and M. Palusiak, *Struct. Chem.,* 2013, 24, 1297–1306.
74 S. C. Nyburg and C. H. Faerman, *Acta Cryst. B,* 1985, 41, 274-279.
75 S. L. Price, A. J. Stone, J. Lucas, R. S. Rowland and A. E. Thornley, *J. Am. Chem. Soc.,* 1994, 116, 4910-4918.
76 J. P. M. Lommerse, A. J. Stone, R. Taylor and F. H. Allen, *J. Am. Chem. Soc.,* 1996, 118, 3108-3116.
77 R. J. Wheatley and A. A. Gopal, *Phys. Chem. Chem. Phys.,* 2012, 14, 2087-2091.
78 P. Politzer, J. S. Murray and T. Clark, *Phys. Chem. Chem. Phys.,* 2010, 12, 7748-7757.
79 L. piela, *Ideas of quantum chemistry,* Elsevier (1st Ed.), Poland, 2007, pp. 615-647.
80 R. Balu, P. Korambath, R. Pandey and S. P. Karna, *Chem. Phys. Lett.,* 2013, 590, 58-62.
81 V. Keshari, S. P. Karna and P. N. Prasad, *J. Phys. Chem.,* 1993, 97, 3525–3529.
82 R. Antonie and V. Bonačić-Kontecký, *Liganded silver and gold quantum clusters. Towards a new class of nonlinear optical nanomaterials*, SpringerBriefs in Materials, 2018, pp. 21-27.
83 P. Parmar, K. A. Peterson and A. E. Clark, *J. Chem. Phys.,* 2014, 141, 234304.
84 D. A. Long, *Raman spectroscopy,* McGraw-Hill, New York, 1977, pp. 46-47.
85 K. J. Miller, *J. Am. Chem. Soc.,* 1990, 112, 8543-8551.
86 D. Rappoport and F. Furche, *J. Chem. Phys.,* 2010, 133, 134105.
87 D. Andrae, U. Häu□ßermann, M. Dolg, H. Ttoll and H. Preuß, *Theoret. Chim. Acta,* 1990, 77, 123-141.
88 T. Yanai, D. Tew and N. Hanly, *Chem. Phys. Lett.,* 2004, 393, 51-57.
89 P. Neogrády, V. Kellö, M. Urban and A. J. Sadlej, Int. *J. Quantum Chem.,* 1998, 63, 557-565.
90 V. Kello and A. J. Sadlej, *Theor. Chim. Acta*, 1992,83, 351.
91 U. Hohm and A. J. Thakkar, *J. Phys. Chem. A*, 2012, 116, 697.
92 S. G. Porsev and A. Derevianko, *J. Exp. Theor. Phys. (JETP)*, 2006, 102, 195.
93 P. Porsev and A. Derevianko, *Phys. Rev. A*, 2002,65, 02701.
94 T. M. Miller, in *CRC Handbook of Chemistry and Physics*, Ed.: D. R. Lide, CRC Press, New York, 2002.
95 G. Doolen (Personal communication August 2003), *Phys. Scr.*, 1987, 36, 77. See also: D. A. Liberman, J. T. Waber and D. T. Cromer, *Phys. Rev.*, 1965.137, A27.
96 V. A. Dzuba, *Phys. Rev. A*, 2016, 93, 032519.
97 M. Seth, P. Schwrrdtfeger and M. Dolg, *J. Chem. Phys.*, 1997, 106, 3623.
98 U. Hohm and K. Kerl, *Mol. Phys.*, 1990, 69, 803-817; ibid. *Mol. Phys.*, 1990, 69, 819-831.
99 G. Maroulis, C. Makris, U. Hohm and D. Goebel, *J. Phys. Chem. A*, 1997, 101, 953.
100 A. D. Becke, *Phys. Rev. A,* 1988, 38, 3098-3100.
101 C. Lee, W. Yang and R. G. Parr, *Phys. Rev. B,* 1988, 37, 785-789.
102 B. Miehlich, A. Savin, H. Stoll and H. Preuss, *Chem. Phys. Lett.,* 1989, 157, 200-206.
103 G. Maroulis, *Chem. Phys. Lett.,* 2007, 444, 44-47.
104 J. Wang, P. Cieplak, R. Luo and Y. Duan, *J. Chem. Theory Comput.,* 2019, 15, 1146–1158.
105 M. Dolg, H. Stoll and H. Preuss, *J. Chem. Phys.,* 1989, 90, 1730-1734.

View Article Online
DOI: 10.1039/D5CP01756D

106 R. Gulde, P. Pollak and F. Weigend, *J. Chem. Theory Comput.,* 2012, 8, 4062–4068.

107 D. A. Pantazis, X. Y. Chen, C. R. Landis and F. Neese, *J. Chem. Theory Comput.*, 2008, 4, 908-919.

108 D. A. Pantazis and F. Neese, *J. Chem. Theory Comput.*, 2009, 5, 2229-2238.

109 D. A. Pantazis and F. Neese, *J. Chem. Theory Comput.*, 2011, 7, 677-684.

110 D. A. Pantazis and F. Neese, *Theor. Chem. Acc.*, 2012, 131, 1292.

111 K. L. Schuchardt, B. T. Didier, T. Elsethagen, L. Sun, V. Gurumoorthi, J. Chase, J. Li and T. L. Windus, *J. Chem. Inf. Model.*, 2007, 47, 1045-1052.

112 B. P. Pritchard, D. Altarawy, B. Didier, T. D. Gibson and T. L. Windus, *J. Chem. Inf. Model.,* 2019, 59, 4814-4820.

113 A. C. Neto and F. E. Jorge, *Chem. Phys. Lett.,* 2013, 582, 158-162.

114 V. Kellö and A. J. Sadlej, *Theoret. Chim. Acta,* 1996, 94, 93–104.

115 M. Reiher, *Theor. Chem. Acc.*, 2006, 116, 241-252.

116 M. Reiher and A. Wolf, *Relativistic quantum chemistry*, Wiley-VCH Verlag GmbH & Co. KGaA, 2015, pp. 469-496.

117 L. Visscher and K. G. Dyall, *At. Data Nucl. Data Tables,* 1997, 67, 207-224.

118 A. Pipertzis, G. Papamokos, M. Mühlinghaus, M. Mezger, U. Scherf and G. Floudas, *Macromolecules,* 2020, 53, 3535-3550.

119 D. F. Parsons and B. W. Ninham, *J. Phys. Chem. A,* 2009, 113, 1141-1150.

120 Gaussian 09 (Revision D.01): M. J. Frisch et al., Gaussian, Inc., Wallingford CT, 2009.

121 ORCA (version 4.2.1): F. Neese, *WIREs: Computational Molecular Science,* 2012, 2, 73–78. Software update: *WIREs: Computational Molecular Science,* 2017, 8, e1327.

122 GaussView (version 6.0.16): R. D. Dennington, T. A. Keith and J. M. Millam, 2000-2016.

123 Multiwfn (version 3.7): T. Lu and F. Chen, *J. Comput. Chem.*, 2012, 33, 580-592.

124 NBO (version 3.1): E. D. Glendening, A. E. Reed, J. E. Carpenter and F. Weinhold, 2001.

125 W. R. Johnson, U. I. Safronova, A. Derevianko and M. S. Safronova, *Phys. Rev. A*, 2008, 77, 022510.

126 M. Puchalski, D. Kedziera and K. Pachucki, *Phys. Rev. A*, 2011, 84, 052518; Erratum: *Phys. Rev. A*, 2012, 85, 019910E.

127 A. Derevianko, W. R. Johnson, M. S. Safronova and J. E. Babb, *Phys. Rev. Lett.*, 1999, 82,3589.

128 C. R. Ekstrom, J. Schmiedmayer, M. S. Chapman, T. D. Hammond and D. E. Pritchard, *Phys. Rev. A,* 1995, 51, 3883-3888.

129 A. Miffre, M. Jacquey, M. Büchner, G. Trénec and J. Vigué, *Phys. Rev. A,* 2006, 73, 011603(R).

130 Y. Tawada, T. Tsuneda, S. Yanagisawa, T. Yanai, and K. Hirao, *J. Chem. Phys.*, 2004, 120, 8425.

131 H. Iikura, T. Tsuneda, T. Yanai and K. Hirao, *J. Chem. Phys.*, 2001, 115, 3540-3544.

132 M. Mantina, A. C. Chamberlin, R. Valero, C. J. Cramer and D. G. Truhlar, *J. Phys. Chem. A,* 2009, 113, 5806-5812.

133 H. Tatewaki, Y. Hatano, T. Noro and S. Yamamoto, *AIP Advances,* 2015, 5, 067142.

134 C. I. Hancox, S. C. Doret, M. T. Hummon, R. V. Krems and J. M. Doyle, *Phys. Rev. Lett.,* 2005, 94, 013201.

135 R. V. Krems, J. Kłos, M. F. Rode, M. M. Szczęśniak, G. Chałasiński and A. Dalgarno, *Phys. Rev. Lett.,* 2005, 94, 013202.

136 M. Tarazkar, D. A. Romanov and R. J. Levis, *J. Phys. B: At. Mol. Opt. Phys.,* 2015, 48, 094019.

137 A. Müller, G. J. P. Deblonde, P. Ercius, S. E. Zeltmann, R. J. Abergel and A. M. Minor, *Nat. Commun.,* 2021, 12, 948.

138 T. M. Miller and B. Bederson, *Adv. At. Mol. Phys.,* 1978, 13, 1-55.

139 A. Mitsopoulos, *Conic sections: A brief introduction,* 2025, CC BY 4.0, 1-15.

140 K. Bansal, *Engineering: Open Access (EOA),* 2023, 1, 60-62.

141 S. Sýkora, E. Byte, V. R. Sanzio and C. Primo, *Approximations of ellipse perimeters*, Stan's library, Ed.: S. Sýkora, Vol. 1, 2005.

142 J. Mitroy, M. S. Safronova and C. W. Clark, *J. Phys. B: At. Mol. Opt. Phys.,* 2010, 43, 202001.

143 M. B. Villarino, *J. Ineq. Pure and Appl. Math.,* 2006, 7, 1- 10.

144 L. Dingle and M. Tooley, *Aircraft engineering principles*, Taylor & Francis, New York (2nd ed.), 2013, pp. 35-37.

145 A. B. Ayoub, *The College Mathematics Journal,* 2003, 34, 116-121.

146 V. C. Dragomir, D. N. Ghitau, M. S. Mihailescu and M. G. Rotaru, *Developments in Solid Earth Geophysics,* 1982, 13, 176.

147 D. D. Laun and C. H. Corliss, *J. Res. Natl. Bur. Stand. A-Phys. Chem.*, 1968, Vol. 72A, 609.

148 P. Pyykkö, *Annu. Rev. Phys. Chem.,* 2012, 63, 45–64.

149 E. Eliav and U. Kaldor, *Phys. Rev. A,* 1994, 49, 1724-1729.

150 P. Pyykkö, *The effects of relativity in atoms, molecules and the solid state,* Springer, Boston MA, 1991, pp. 1-13.

151 E. M. Fernández, J. M. Soler, I. L. Garzón and L. C. Balbás, *Phys. Rev. B,* 2004, 70, 165403.

152 L. Xiao and L. Wang, *Chem. Phys. Lett.,* 2004, 392, 452-455.

153 D. Ganyushin and F. Neese, *J. Chem. Phys.*, 2013, 138, 104113.

154 A. V. Y. D. Deyne, E. Pauwels, V. V. Speybroeck and M. Waroquier, *Phys. Chem. Chem. Phys.*, 2012, 14, 10690-10704.

155 F. Neese, *J. Chem. Phys.*, 2005, 122, 034107.

156 R. M. Elliott and J. Wulff, *Phys. Rev.,* 1939, 55, 170-175.

157 H. Yakobi, E. Eliav and U. Kaldor, *J. Chem. Phys.,* 2007, 126, 184305.

158 N. J. Stone, *Table of nuclear electric quadrupole moments*, Oxford physics, 2021, p. 9.

159 H. Haken and H. C. Wolf, *The physics of atoms and quanta: Introduction to experiments and theory,* Springer-Verlag, Berlin Heidelberg (6th ed.), 2000, p. 369.

160 A. J. Sadlej, M. Urban and O. Gropen, *Phys. Rev. A*, 1991, 44, 5547.

View Article Online
DOI: 10.1039/D5CP01756D

Data Avalability:

The data supporting this article have been included as part of the ESI.